2003

A Large-Scale Seasonal Modeling Study of the California Current System

Batteen, Mary L.; Cipriano, Nicholas J.; Monroe, James T.

Journal of Oceanography, Vol. 59, pp. 545 to 562, 2003
https://hdl.handle.net/10945/47158

Journal of Oceanography, Vol. 59, pp. 545 to 562, 2003

A Large-Scale Seasonal Modeling Study of the California Current System

MARY L. BATTEEN*, NICHOLAS J. CIPRIANO and JAMES T. MONROE

Department of Oceanography, Naval Postgraduate School, Monterey, CA 93943, U.S.A.

(Received 13 November 2000; in revised form 6 January 2003; accepted 7 January 2003)

A high-resolution, multi-level, primitive equation ocean model has been used to investigate the combined role of seasonal wind forcing, seasonal thermohaline gradients, and coastline irregularities on the formation of currents, meanders, eddies, and filaments in the entire California Current System (CCS) region, from Baja to the Washington-Canada border. Additional objectives are to further characterize the meandering jet south of Cape Blanco and the seasonal variability off Baja. Model results show the following: All of the major currents of the CCS (i.e., the California Current, the California Undercurrent, the Davidson Current, the Southern California Countercurrent, and the Southern California Eddy) as well as filaments, meanders and eddies are generated. The results are consistent with the generation of eddies from instabilities of the southward current and northward undercurrent via barotropic and baroclinic instability processes. The meandering southward jet, which divides coastally-influenced water from water of offshore origin, is a continuous feature in the CCS, and covers an alongshore distance of over 2000 km from south of Cape Blanco to Baja. Off Baja, the southward jet strengthens (weakens) during spring and summer (fall and winter). The area off southern Baja is a highly dynamic environment for meanders, filaments, and eddies, while the region off Point Eugenia, which represents the largest coastline perturbation along the Baja peninsula, is shown to be a persistent cyclonic eddy generation region.

Keywords:
· California Current,
· eastern boundary currents,
· numerical modeling,
· ocean modeling,
· coastal circulation,
· mesoscale eddies.

1. Introduction

The California Current System (CCS) is a classical eastern boundary current (EBC) system located off the west coast of North America extending approximately from the Strait of Juan de Fuca southward to the tip of the Baja Peninsula (Hickey, 1998). As in other EBC regimes, satellite infrared sea surface temperature (SST) imagery of the CCS (e.g., Strub *et al*., 1990, 1991) has revealed a complex flow structure with seasonal variations. Dominant mechanisms responsible for the observed large-scale structure within the CCS have been shown to be seasonal variations in alongshore wind stress (Bakun and Nelson, 1991), coastline irregularities (e.g., Batteen, 1997), bottom topography (e.g., Ikeda *et al*., 1984), and temperature and salinity variations (Batteen *et al*., 1995; Batteen and Vance, 1998).

The CCS is comprised of several large-scale (>500 km) alongshore currents including the California Current (CC), the California Undercurrent (CUC) and the Davidson Current (DC) (Fig. 1). The predominant flow is the CC, which is a broad (~1000 km offshore), shallow (surface to ~500 m), relatively slow (~10 cm/s), year-round southward current. The CUC is a relatively narrow (~10–40 km width), weak (~2–10 cm/s), subsurface northward flow which is strongest at ~100–300 m depth and varies seasonally. The DC is a weak, inshore, surface flow north of Point Conception which flows northward during fall and winter. Other northward surface flows include the Southern California Countercurrent (SCC) south of Point Conception and the Southern California Eddy (SCE) shoreward of the Channel Islands within the Southern California Bight (Hickey, 1979, 1998).

Studies using satellite imagery (e.g., Bernstein *et al*., 1977; Chelton, 1984; Strub *et al*., 1991) have shown that the CCS is not the stable system of currents with the well-defined, unchanging structure suggested by Fig. 1. Rather, within the mean, large-scale structure of the CCS there exist perturbations in the form of mesoscale meanders, eddies, and filaments, which vary both spatially and temporally. Numerical modeling efforts by Batteen (1997)

* Corresponding author. E-mail: mlbattee@nps.navy.mil

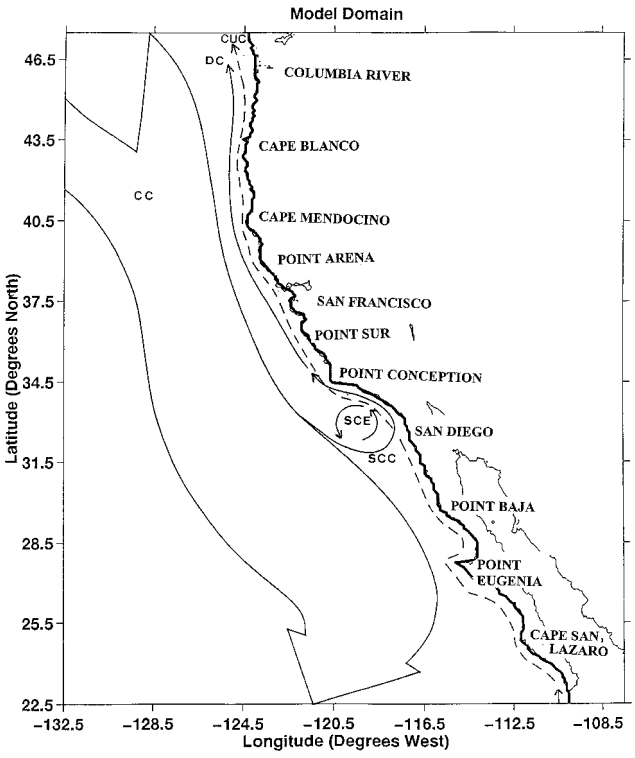

Fig. 1. Model domain, coastline, and generalized classical circulation of the California Current System (CCS). The domain is bounded by 22.5°N to 47.5°N, 107.5°W to 132.5°W. The broad, slow surface southward California Current (CC) overlies the narrow, northward California Undercurrent (CUC). Surface southward flows include the Davidson Current (DC) north of Point Conception, and the Southern California Eddy (SCE) and Southern California Countercurrent (SCC) south of Point Conception.

simulated this complex eddy-mean flow interaction within the northern CCS using a high-resolution, multi-level, primitive equation (PE) ocean model, emphasizing the role of wind-forcing and coastline irregularities. Specifically, the seasonal variation of the alongshore component of wind stress was shown to be critical in generating realistic horizontal and vertical structures for the surface southward CC and the subsurface northward CUC. Both baroclinic and barotropic instability mechanisms contributed to the generation of meanders, filaments, and eddies. Additionally, coastline irregularities were shown to help "anchor" upwelling filaments and to enhance the growth of meanders and eddies. In particular, the region off Cape Blanco was identified as the location where the inshore edge of the CC leaves the coast and develops a meandering jet to the south. Other studies with coastline irregularities and/or bottom topography (e.g., Ikeda *et al.*, 1984; Haidvogel *et al.*, 1991) also showed that while bottom topography and/or coastline irregularities can enhance the growth of instabilities, the basic instability still results from the opposing alongshore currents. In recent observational (Batteen *et al.*, 1995) and modeling studies (Batteen and Vance, 1998) on the combined effect of temperature and salinity on density, it was shown that, even though the effects of wind forcing dominate the CCS, the additional effects of thermohaline gradients are important in defining the large-scale structure and circulation of the CCS. Although the modeling study of Batteen and Vance (1998), which included wind forcing, coastline irregularities, and thermohaline gradients, was able to reproduce some of the currents in the CCS (i.e., the CC and CUC), the model did not generate the DC, SCC, or SCE which are thought to originate south of the model domain used by Batteen and Vance (1998).

In this study, the model of Batteen (1997) and Batteen and Vance (1998), originally restricted to the latitudes poleward of 35°N, is expanded by extending the model domain southward to 22.5°N. As a result, the entire CCS region from Baja to the Washington-Canada border is included, which allows the generation of all of the major currents of the CCS shown in Fig. 1 as well as filaments, meanders, and eddies.

Besides investigating the combined role of seasonal wind forcing, thermohaline gradients, and a realistic coastline in the generation of these features, a key issue that has not yet been resolved is addressed using the results of the model simulations. This issue is the seasonal variability off the Baja peninsula, which, with the possible exception of northern Baja (which has been regularly sampled by the California Cooperative Fisheries Investigation, CalCOFI, and covers the region north of Point Baja to the U.S.-Mexico border), remains a data sparse region with a poorly known seasonal cycle (Hickey, 1998).

2. Model Forcing Conditions and Energy Analysis Technique

The model ocean is essentially the same as the PE model described by Batteen (1997) and Batteen and Vance (1998), and so only a brief description of the forcing conditions and experimental design for the expanded model domain is presented here. The model domain (Fig. 1) encompasses the west coast of the United States and the Baja Peninsula, from 22.5°N to 47.5°N (2816 km alongshore), and from 107.5°W to 132.5°W offshore (2304 km cross-shore). Bottom topography has been omitted to focus on the roles of seasonal wind forcing, seasonal thermohaline gradients, and coastline irregularities. (The additional inclusion of bottom topography and its effects on the CCS are considered a separate study.) The eastern boundary is modeled as a coastal wall. The constant depth used in the model is 4500 m.

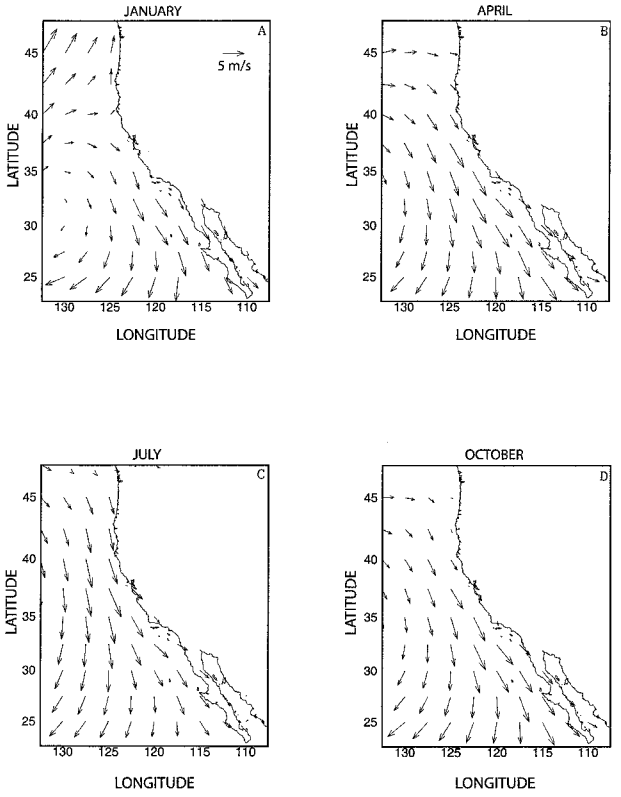

Fig. 2. Climatological winds over the California Current System used to force the model. The climatological (1980–1989) ECMWF winds are shown here for (a) January, (b) April, (c) July, and (d) October.

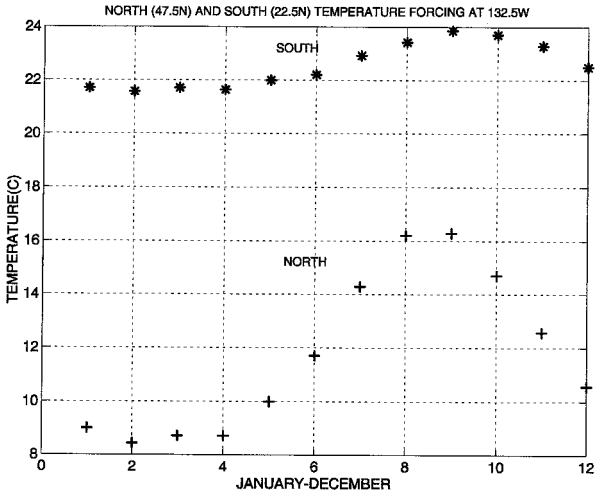

Fig. 3. Time series plots of monthly temperature fields used as seasonal forcing in the basic simulation. The "*" symbol represents data at 22.5°N, 132.5°W, while the "+" symbol represents data at 47.5°N, 132.5°W for 13 m depth.

2.1 Model forcing conditions

The effects of seasonal wind forcing are included using monthly varying climatological wind fields from the European Centre for Medium-Range Weather Forecasts (ECMWF) near-surface wind analyses from 1980–1989 (Trenberth *et al.*, 1990). Note that the use of monthly varying climatological winds allows the seasonal cycle of winds to be isolated and explored (forcing with daily winds, weekly winds, or winds with interannual variability are considered in separate studies). The wind fields, which are on a 2.5 × 2.5 degree grid, have been interpolated spatially to the 9 × 11 km model resolution.

Sample monthly wind fields used in the study are shown in Fig. 2, which depicts the seasonal influence and migration of flow around the North Pacific Subtropical High over the area encompassed by the model domain. Figure 2(a) shows a divergence of flow at the coast in the vicinity of ~40°N during the winter as the winds circulate anticyclonically around the Subtropical High to the south and cyclonically around the Aleutian Low to the north. By spring (Fig. 2(b)), the Subtropical High has begun its westward and northward expansion, producing increased southward winds over most of the model domain and causing the divergence of flow to move north to ~44°N, off the Washington coast. In July (Fig. 2(c)), southward, upwelling-favorable winds dominate along the entire coastline as the Subtropical High reaches its maximum extent. Figure 2(d) shows a decrease in magnitude of southward winds during fall as the Subtropical High begins to recede southward.

The effects of thermohaline gradients in the CCS are incorporated using monthly temperature and salinity climatology from Levitus *et al*. (1994) and Levitus and Boyer (1994). Forcing occurs over the upper seven levels, which are initially assumed to be zonally homogeneous. Since the lower three levels do not exhibit any significant horizontal variation in temperature and salinity, constants are assumed for each level. Temperature values used for levels 8 (1416 m), 9 (2283 m), and 10 (3656 m) are 2.56°C, 2.08°C, and 2.00°C, respectively, while the salinity constant used for the lower three levels is 34.7. Only the upper layer (13 m and 46 m) temperature forcing conditions for the northern (47.5°N) and southern (22.5°N) boundaries show significant seasonal variability, with a temperature maximum in late summer to early fall and a minimum in late winter to early spring throughout the region (e.g., Fig. 3). Below these depths, both the seasonal temperature fluctuations and temperature gradient weaken. Conversely, salinity forcing conditions at all seven levels, which show less (more) saline water to the north (south), have no significant seasonal cycle (not shown). The monthly values of temperature and salinity at the western boundary (132.5°W) have been linearly interpolated to daily values and are used to force the model once a day.

The design of the study is as follows. A realistic North American coastline is used to include the effects of irregular coastline geometry over the entire CCS region. Model integrations start from a state of rest. The model is updated once a month with the seasonal ECMWF winds. At the western boundary the model is updated daily with the seasonal temperature and salinity fields. The model is run for three years to allow it to reach a state of quasi-equilibrium.

2.2 Energy analysis techniques

The energy analysis technique used is the same as that used and described by Batteen *et al*. (1992) and is based on that of Han (1975) and Semtner and Mintz (1977). This analysis is done to gain a better understanding of the types of energy transfer during unstable flow in the CCS. A brief summary of the method follows.

Kinetic energy is calculated for the horizontal components. After a quasi-steady state is reached in which the total kinetic energy is nearly constant, the time mean kinetic energy (MKE) and eddy kinetic energy (EKE) are calculated using the sum of squared mean and horizontal fields, respectively. Next, the available potential energy is calculated and used to determine when a quasi-steady state is reached and when statistics should be collected. The temporal mean and eddy available potential energies are then computed. The baroclinic and barotropic energy transfers, defined by Batteen *et al*. (1992), are used to argue for the type of instability mechanism (e.g., baroclinic, barotropic, or mixed) leading to the initial eddy generation (see the Appendix for a more complete description of the calculations used in the energy analysis technique).

3. Results

3.1 Spin-up phase

Due to the combination of thermohaline gradients and wind forcing, different oceanic responses are expected and occur in the CCS depending on the season, i.e., depending on whether it is winter, the upwelling season (~April to September), or the fall. Here we describe the different oceanic responses for each season.

In the winter, in the northward end of the model domain, the large meridional high to low atmospheric pressure gradient due to the decrease of temperature northward (Fig. 3) establishes an onshore geostrophic flow, while the northward wind stress results in an onshore Ekman flow. On approaching the eastern boundary, the onshore flow turns and forms a northward coastal current (e.g., Fig. 4(a)). In the southward end of the model domain the smaller pressure gradient (due to the smaller warm to cold temperature gradient) and the southward wind stress results in weak onshore geostrophic flow, offshore Ekman flow, and a coastal southward surface current (e.g., Fig. 5(a)). Typical cross-sections of meridional velocity taken to the north (Fig. 6(a)) and south (Fig. 7(a)) show, in the north (south), a predominantly northward (southward) flow overlying an inshore southward (northward) flow.

During the upwelling season, the combination of a weakened pressure gradient and increased southward winds over the entire model domain lead to a strengthening of southward flow all along the coast and a weakening (strengthening) of onshore (offshore) flow. A southward coastal jet is discernible as a relatively narrow coastal flow in the north (e.g., Fig. 4(b)). Due to the presence of irregular coastline features such as capes, the jet broadens in scope as it progresses southward (e.g., Fig. 5(b)). Maximum speeds in the northern half of the domain are ~20 cm/s whereas current speeds associated with cyclonic eddy activity in the south are ~30–50 cm/s. There is also an inshore northward undercurrent with maximum speeds of ~15–20 cm/s which can be traced northward across the entire model domain (not shown). Typical cross-sections of meridional velocity taken to the north (Fig. 6(b)) and south (Fig. 7(b)) show the vertical structure of the currents with southward flow overlying a northward undercurrent.

As the coastal jet and undercurrent become fully established (from day ~180 to day ~285), the currents become unstable and form meanders (e.g., Figs. 4(c) and 5(c)) as well as cold, upwelling filaments (not shown). As the meanders intensify, eddies are formed in the coastal, southward region of the domain (e.g., Fig. 5(c)). The eddies are predominantly cold core and cyclonic, on the order of 100 km in diameter, and regularly extend to ~50–100 km off the coast. Throughout the upwelling season, which corresponds to the period of maximum southward wind stress (Fig. 2), meanders, filaments, and eddies continue to develop southward of ~44°N (not shown).

In the fall, the Aleutian Low begins to deepen and the Subtropical High migrates toward its wintertime position in the south. With this transition, northward wind stress returns to the northern portion of the model domain as the regional pressure gradient strengthens. A typical cross-section of meridional velocity taken to the north (Fig. 6(c)) illustrates that during this transition the northward undercurrent surfaces while the surface coastal southward jet moves offshore. In the southern part of the model domain, as in the other seasons, the surface coastal southward current continues to overlie the northward undercurrent (Fig. 7(c)).

3.2 Quasi-equilibrium phase

Longer run times (~3 years) with model output fields averaged every 3 days for the months of January, April, July, and October illustrate the seasonal variability and

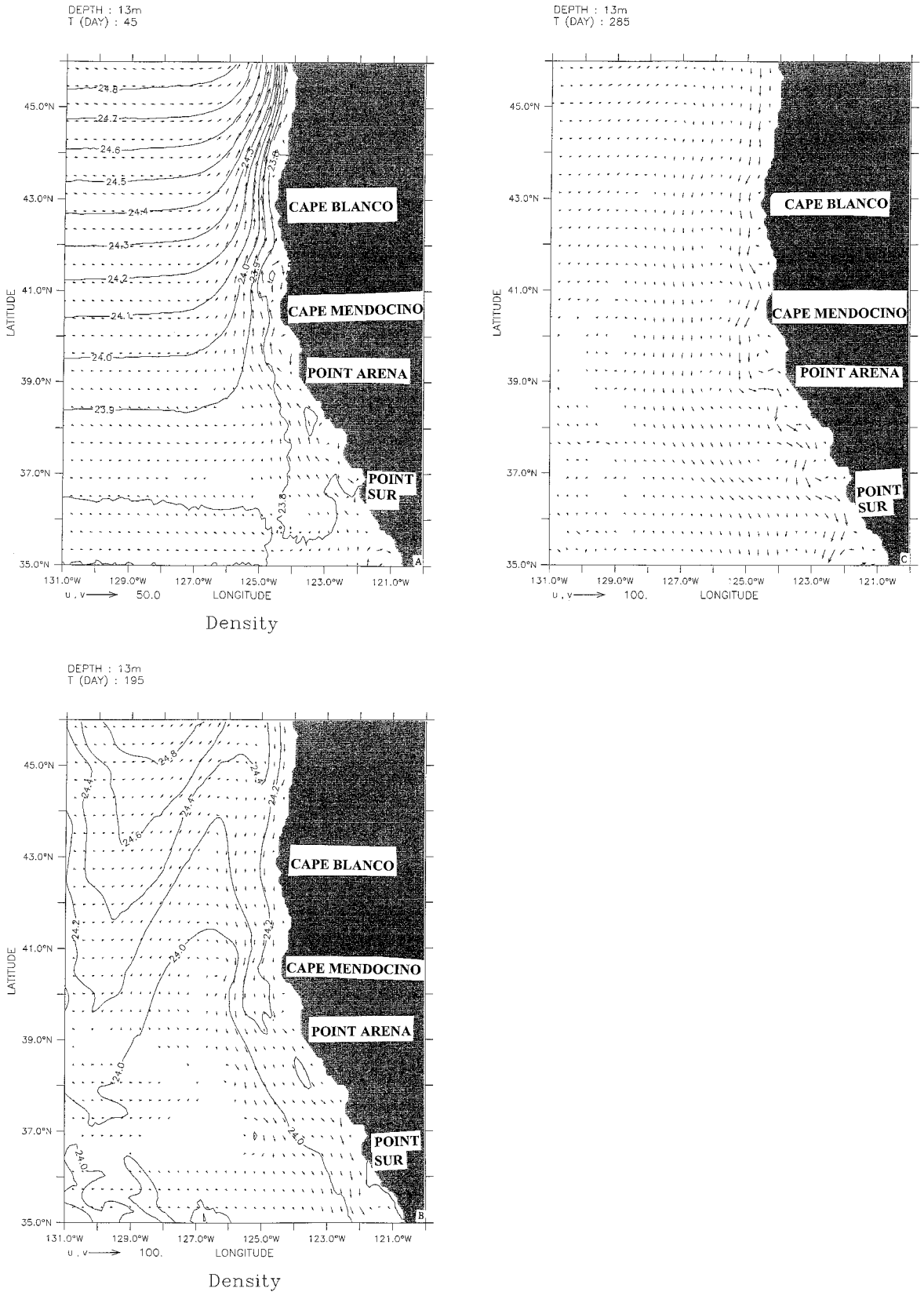

Fig. 4. Velocity vectors at 13 m depth in the northern half of the model domain at days (a) 45, (b) 195, and (c) 285. Maximum velocity vector is 50 cm/s in (a) and 100 cm/s in (b). Density contours are also shown in (a) and (b). Contour interval is 0.1 g/cm^3 in (a) and 0.2 g/cm^3 in (b).

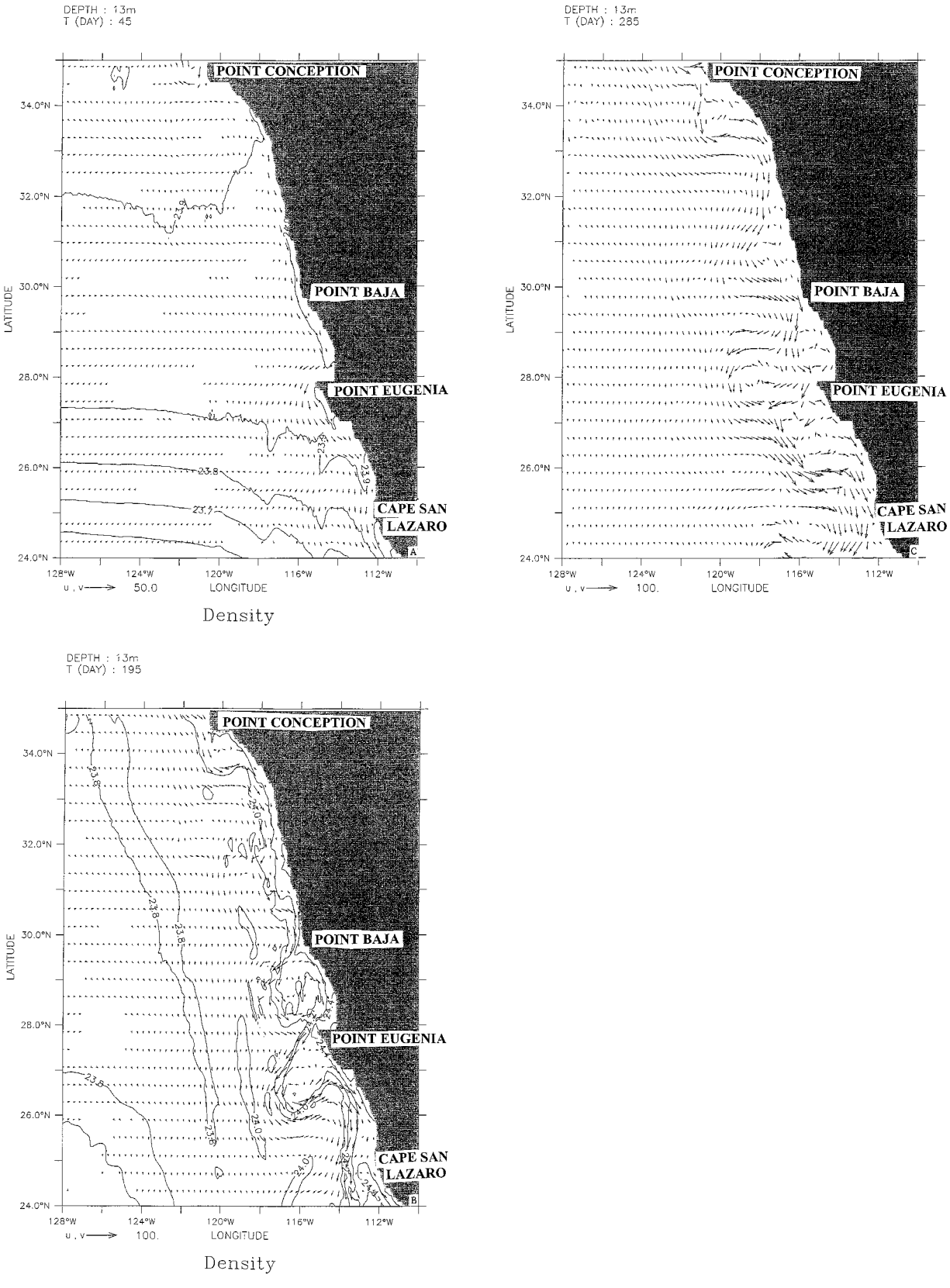

Fig. 5. Velocity vectors at 13 m depth in the southern half of the model domain at days (a) 45, (b) 195, and (c) 285. Maximum velocity vector is 50 cm/s in (a) and 100 cm/s in (b). Density contours are also shown in (a) and (b). Contour interval is 0.1 g/cm^3 in (a) and 0.2 g/cm^3 in (b).

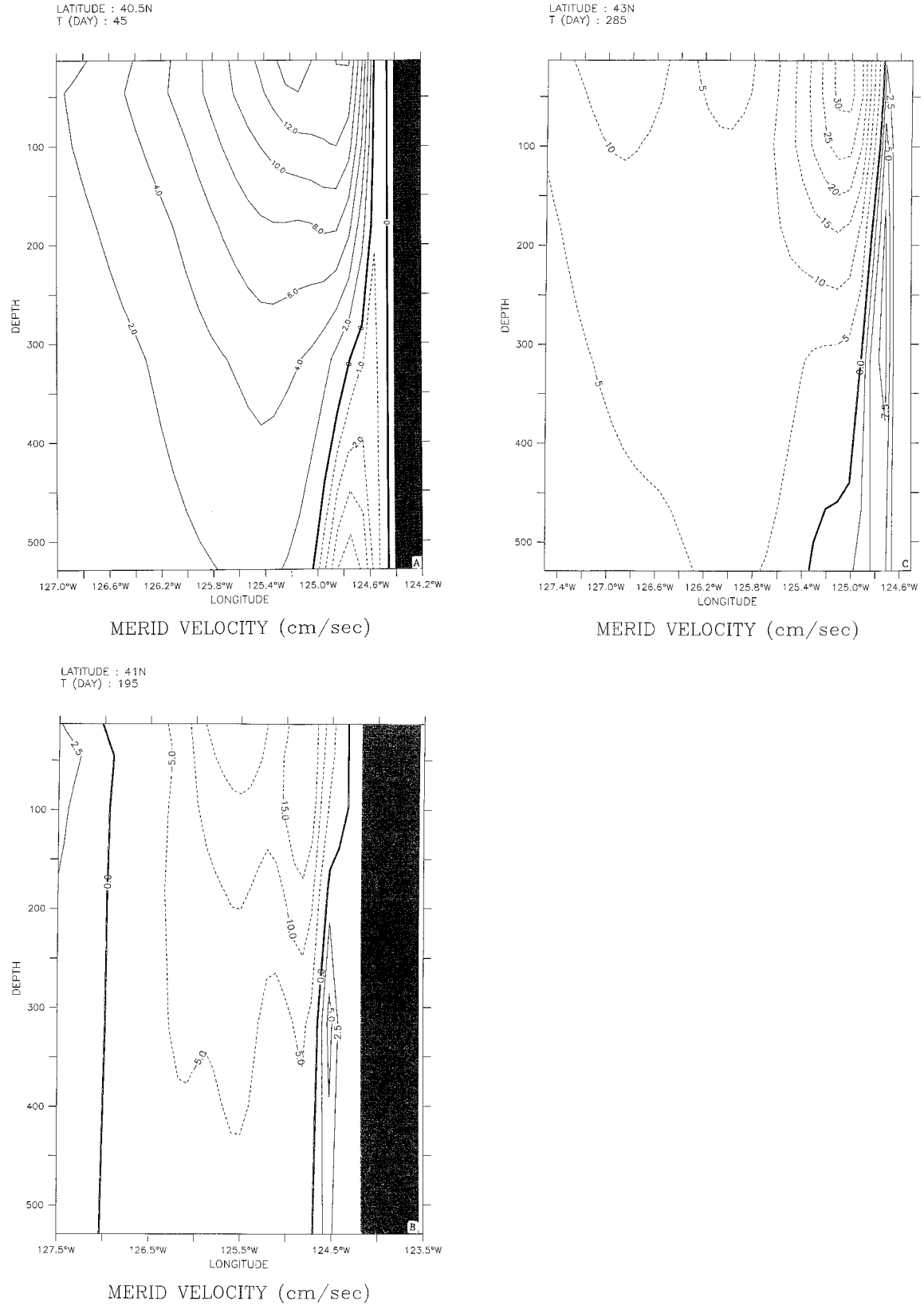

Fig. 6. Cross-shore sections of meridional velocity (v) at (a) 40.5°N (off Cape Mendocino) on day 45, (b) 41°N on day 195, and (c) 43°N on day 285. Northward (southward) flow is denoted by solid (dashed) lines. The contour interval is 2 cm/s (2 cm/s) for northward (southward) flow in (a), and 2.5 cm/s (5 cm/s) for northward (southward) flow in (b) and (c).

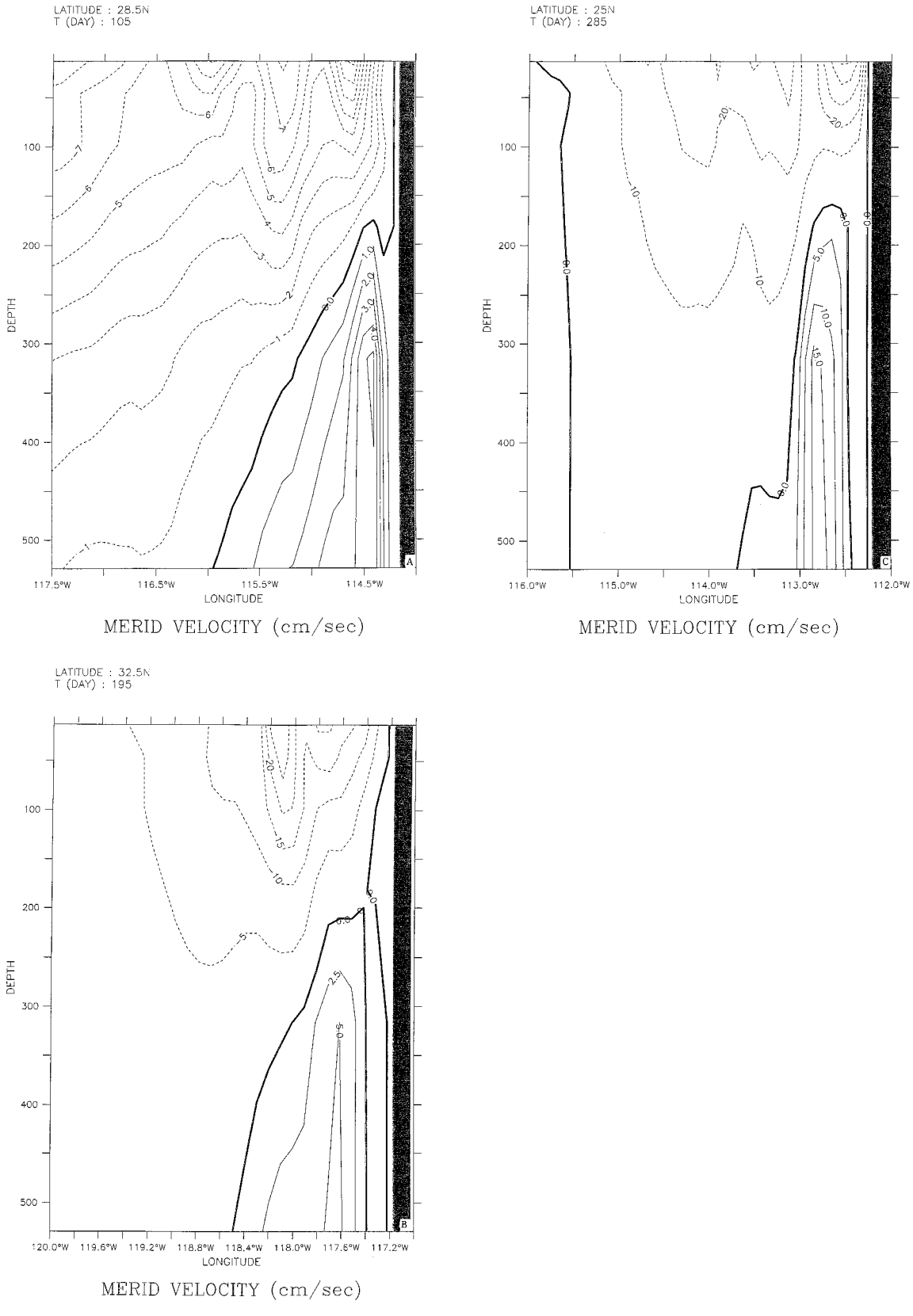

Fig. 7. Cross-shore sections of meridional velocity (v) at (a) 28.5°N (north of Point Eugenia) on day 105, (b) 32.5°N on day 195, and (c) 25°N on day 285. Northward (southward) flow is denoted by solid (dashed) lines. The contour interval is 1 cm/s in (a), 2.5 cm/s (5 cm/s) for northward (southward) flow in (b), and 5 cm/s (10 cm/s) for northward (southward) flow in (c).

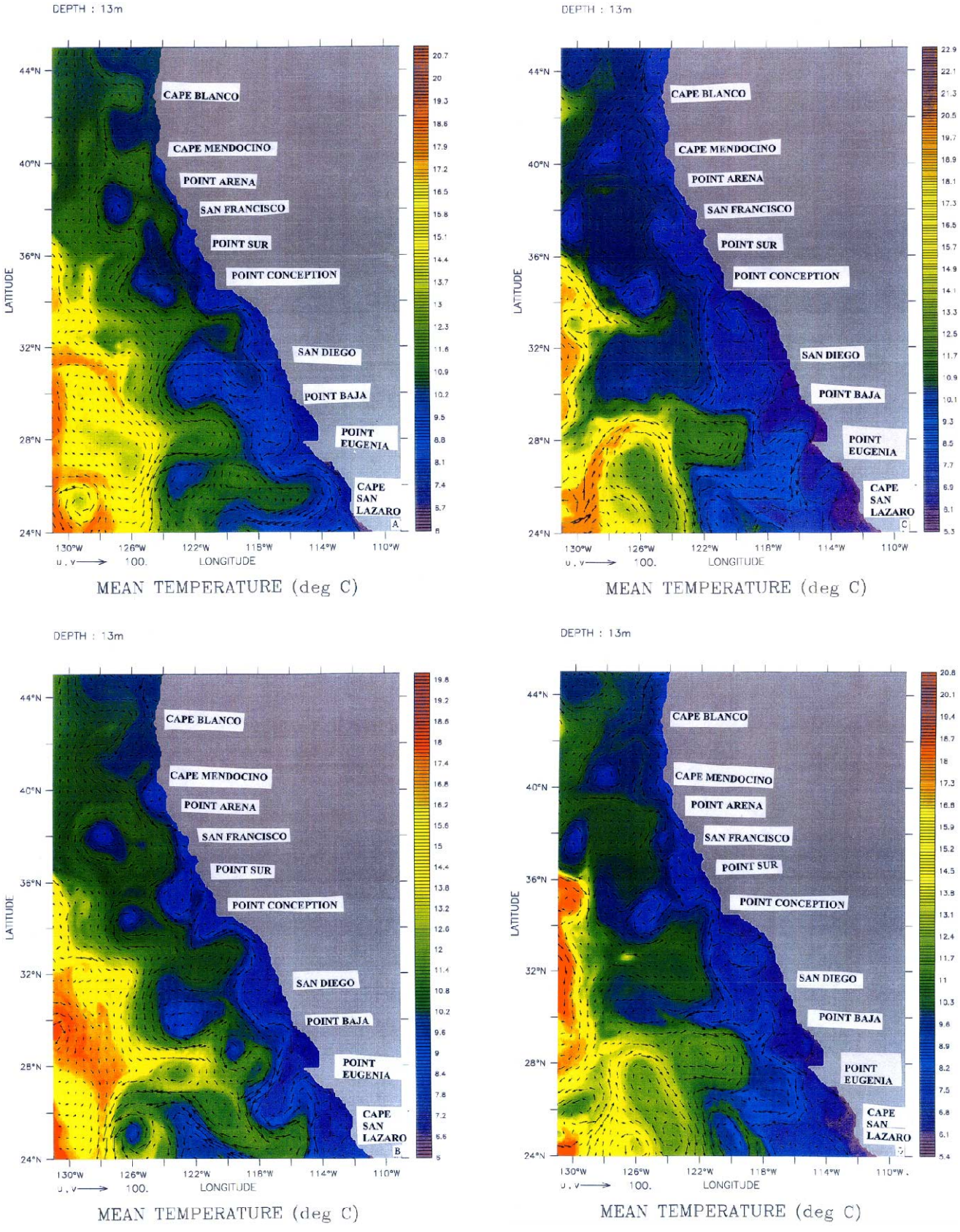

Fig. 8. Mean temperature and velocity vectors at 13 m depth for (a) January, (b) April, (c) July, and (d) October of model year 3. Contour interval is 0.1°C; maximum velocity vector is 100 cm/s.

complex structure of the CCS. By year 3, the model CC core takes the form of a meandering jet embedded with numerous eddies and upwelling filaments (Figs. 8(a)–(d)). Although the mean direction of the CC remains southward near the surface, the circulation contains large zonal components with relatively intense onshore and offshore transports.

Model results show that in winter (e.g., Fig. 8(a), flow at the coast meanders southward and advects colder water near the coast offshore and warmer water from the west onshore throughout the model domain. Both cyclonic and anticyclonic eddies exist on either side of the southward coastal jet and closed, cold-core eddies on the order of 100 km in diameter are present off San Francisco at ~38°N, 126°W, and in the southwest corner of the domain at ~25°N, 129.5°W. The coldest water found in the model is located adjacent to the southern Baja coastline coincident with persistent northwesterly winds due to the wintertime position of the Subtropical High (Fig. 2(a)). Average current speeds of the southward surface jet range from ~10–50 cm/s, consistent with observations of the CC using drifters (Davis, 1985).

In spring (e.g., Fig. 8(b)), meander activity is more pronounced along the model coastline and more closed eddies exist offshore within the core of the southward model CC. Eddies present in January have propagated westward at speeds of ~1–3 km/day, consistent with Rossby wave propagation speeds. In the north, the inshore surface current has reversed in direction from northward to southward flow. In the south, the coldest water has moved north up the Baja and Southern California coastline in conjunction with the seasonal migration of the Subtropical High and subsequent expansion of upwelling-favorable winds. Also in the south, model results show an increase in magnitude of the southward surface jet from speeds present in January, consistent with observations of the CC using CalCOFI data (Lynn and Simpson, 1987).

In summer (e.g., Fig. 8(c)), temperatures adjacent to the coast in the northern portion of the model (i.e., above ~40°N) have decreased as upwelling-favorable winds now approximately parallel the coastline throughout the domain (Fig. 2(c)). Evidence of cold, offshore-flowing, upwelling filaments exists in the vicinity of Cape Blanco, Cape Mendocino, south of Point Sur, in the Southern California Bight, and below Point Eugenia. These filaments extend ~80–200 km offshore and merge with the meandering southward jet that has speeds of ~30–50 cm/s and alongshore wavelengths of ~100–300 km, consistent with the findings of Brink and Cowles (1991). During the summer the undercurrent develops and spreads north, giving rise to the strong vertical shear and the nonlinear nature of the instabilities in summer. An example of a mesoscale disturbance embedded within the CCS is illustrated by the cyclonic meander that forms off Point Eugenia in January (Fig. 8(a)), intensifies in April (Fig. 8(b)), and breaks away by July (Fig. 8(c)) to propagate southwestward in the CC. Bernstein *et al.* (1977) noted similar mesoscale activity off Point Eugenia using data from CalCOFI surveys of the CCS taken from April to July, 1952. In the vicinity of ~32.5°N within the Southern California Bight, a division of flow is evident, consistent with the report by Reid (1963), in the southward jet as a portion of the jet turns shoreward (Fig. 8(c)). This division of flow is consistent with the summertime formation of the SCE (Lynn and Simpson, 1987).

The spring and summer results are in good agreement with recent satellite imagery (Strub *et al.*, 1991; Strub and James, 1995), field studies using Lagrangian drifters (Barth *et al.*, 1994; Barth and Smith, 1996a, b), and with the hypothesis that the offshore separation of the southward coastal jet in the vicinity of Cape Blanco marks the start of a continuous meander along a temperature front that can be traced southward throughout the entire CCS during spring and summer. By spring (e.g., Fig. 8(b)), when the predominant wind direction transitions southward across the entire CCS, the maximum southward flow off the Oregon coast wanders southwestward in the vicinity of Cape Blanco and subsequently turns shoreward to meander near the coast of Cape Mendocino. The flow then undergoes alternating offshore and onshore excursions, shedding westward-propagating eddies which form a temperature front near the coast, as it proceeds southward. By summer (e.g., Fig. 8(c)), an upwelling front has formed inshore north of Cape Blanco and remains relatively uniform in association with only mild variations in coastline orientation. South of Cape Blanco, the region of cold water near the coast gradually widens with distance southward as coastal water is pulled farther offshore with increased meander activity.

By early fall (e.g., Fig. 8(d)), as the upwelling system begins to weaken with the southward migration of the Subtropical High, the sharp nearshore temperature front present during summer north of Cape Blanco has become more diffuse. The coastal southward surface jet in this region is now oriented farther offshore and embedded streams of colder water flow southwestward into a cold-core eddy west of Cape Mendocino. South of Point Conception, the division of flow is more pronounced as a branch of the southward surface jet rotates onshore and northward while the main portion of the jet continues southward offshore. This flow structure within the Southern California Bight coincides with a seasonal maximum in the SCE from summer to early fall (Hickey, 1998). As in January (Fig. 8(a)), in the vicinity of Point Eugenia, a cyclonic meander in the southward jet is discernible. In time (not shown), this meander intensifies, closes off, and propagates southwestward through the stream.

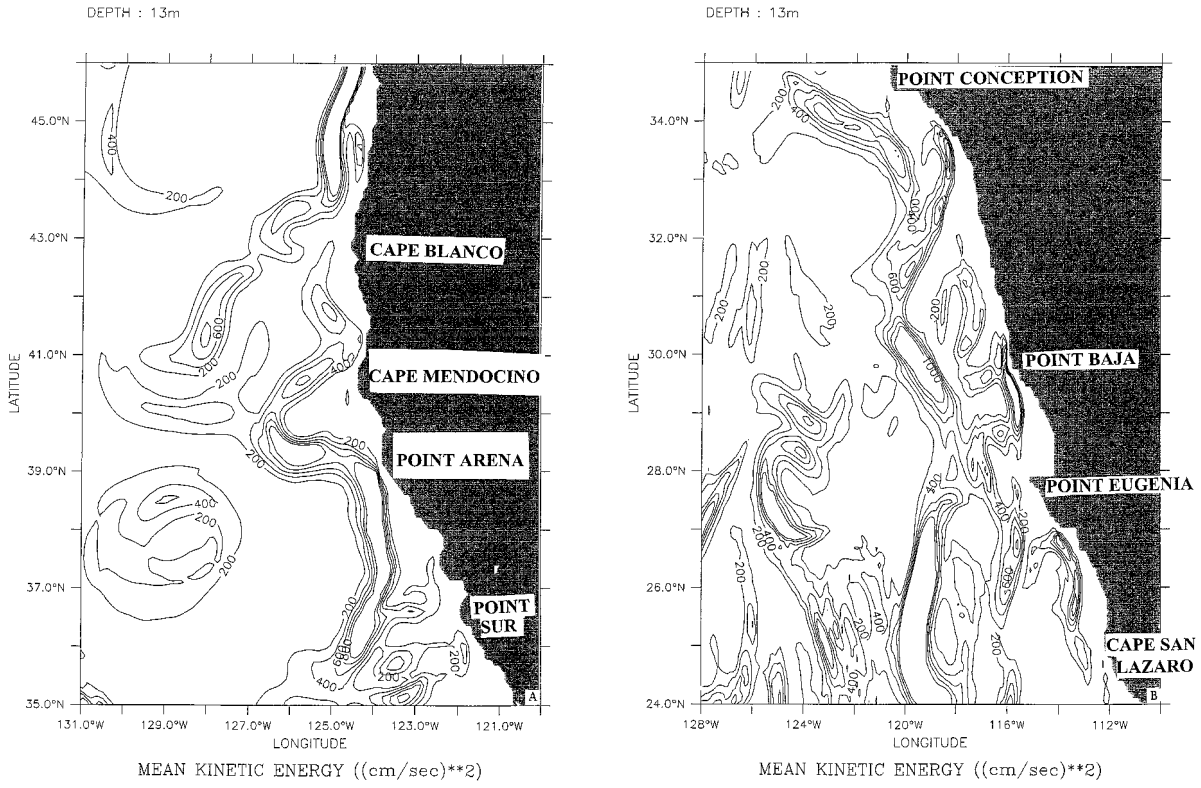

Fig. 9. Horizontal maps at 13 m depth of mean kinetic energy (MKE) for the northern (a) and southern (b) portions of the domain in model year 3 averaged for the month of July. Contour interval is 200 cm^2/s^2.

3.3 Analysis of energetics

Horizontal maps of the upper layer mean kinetic energy (MKE) and eddy kinetic energy (EKE) suggest where the mean and eddy energy sources are to be found (Holland *et al*., 1983). Using Eqs. (A2) and (A3) in the Appendix, maps of MKE and EKE have been averaged monthly in the quasi-equilibrium phase.

A comparison of maps of MKE (e.g., Figs. 9(a) and (b)) with the corresponding mean velocity field (Fig. 8(c)) shows that high values of MKE are found along the coastal and offshore axes of the meandering southward jet, and in the offshore regions south of ~43°N. Regions of high model EKE values (e.g., Figs. 10(a) and (b)) are shown off Cape Blanco, offshore and downstream of Cape Mendocino, Point Arena, and Point Baja, in the Southern California Bight, and in the coastal indentations on either side of Point Eugenia. These regions of high model EKE values correspond to areas where eddies are likely to be generated. Maps of EKE for each month during the upwelling season (not shown) depict higher values of EKE present during late summer. For example, the maximum values of EKE for the eddy located at ~38°N, 129°W in July increased from ~25–50 cm^2/s^2, (Fig. 10(a)), to ~75 cm^2/s^2 by September (not shown).

A comparison of MKE (Fig. 9) with EKE (Fig. 10) shows that maximum MKE and EKE values generally occur in the same vicinity. Note that the MKE values are generally larger than the EKE values. This is consistent with the results of the model simulations, which show that eddies are generated from instabilities of the mean CC and CUC via baroclinic and/or barotropic instability processes.

Kelly *et al*. (1998) examined altimeter, moored ADCP, and drifter data for the CCS to determine the spatial and temporal structure of eddy fields and to investigate the variability of near-surface EKE in the CCS west of 124°W between 33°N–40.5°N. A qualitative and quantitative comparison of EKE results from the present study shows a good correlation with their observations. Both the findings of Kelly *et al*. (1998) and the model results show higher values of EKE in late summer to early fall between ~36°N–40°N and west of ~124°W, coincident with increased southward flow, along with minimum values in the spring (not shown). Specifically, maximum (minimum) EKE values observed by Kelly *et al*. (1998) within their study area were ~200 cm^2/s^2 (100 cm^2/s^2) while maximum (minimum) values in the model were ~300 cm^2/s^2 (100 cm^2/s^2). These values are also similar

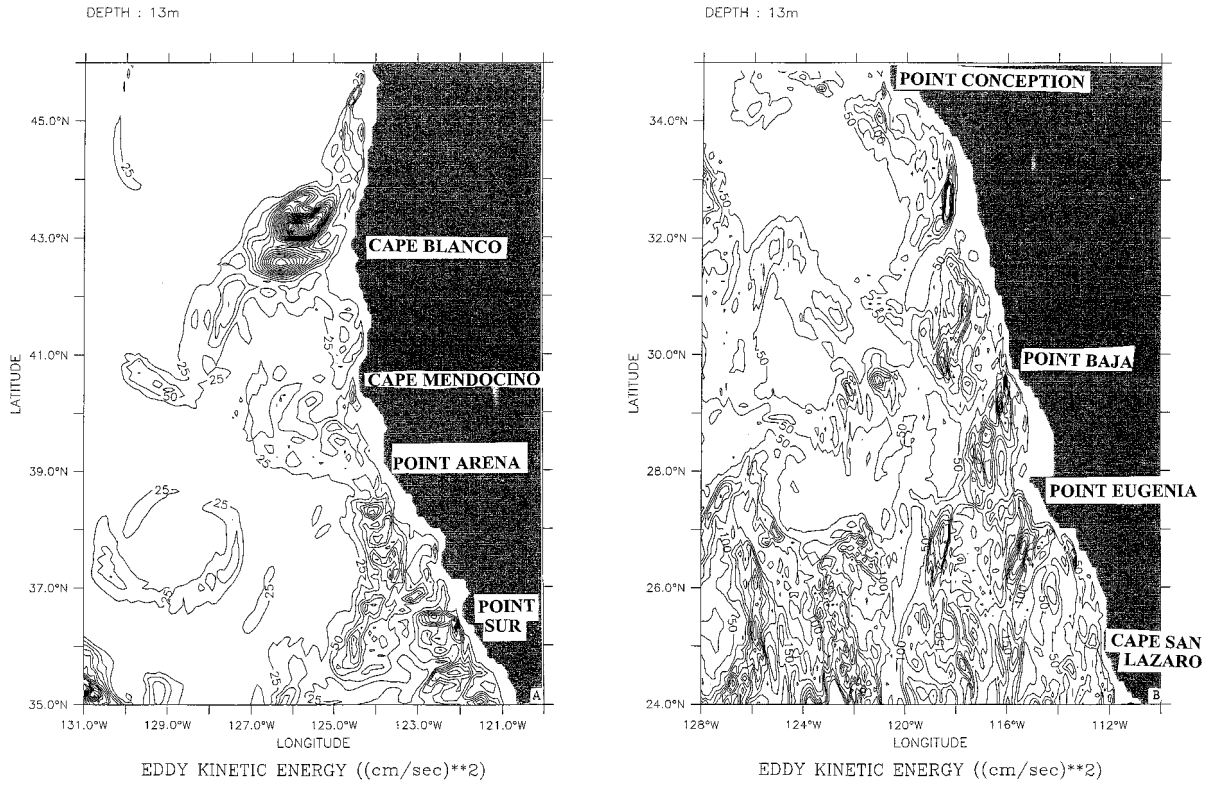

Fig. 10. Horizontal maps at 13 m depth of eddy kinetic energy (EKE) for the northern (a) and southern (b) portions of the domain in model year 3, averaged for the month of July. Contour interval is 25 cm^2/s^2.

to Strub *et al*. (1997). Additionally, both studies reveal a tendency of EKE maxima to propagate westward in time. For example, a time series of EKE from July (Fig. 10(a)) to October (not shown) shows that the offshore EKE maxima have propagated westward or southwestward in time. Thus, the results of the model instability analysis are consistent with the report of Kelly *et al*. (1998).

4. Seasonal Variability off the Baja Peninsula

An additional goal of this study is to utilize model results to address a key issue that has not yet been resolved, viz., to address the seasonal variability off the Baja peninsula, which remains a data-sparse region with a poorly known seasonal cycle (Hickey, 1998).

Lynn and Simpson (1987) have described the flow and water mass characteristics off the Baja Peninsula based on analyses of 23 years of CalCOFI data. Surface southward flow is strongest along the coast, showing significant seasonal variability, with maximum flow of ~20 cm/s occurring in March and April. This inshore equatorward flow is present most of the year with no spring transition as observed north of the border. The near-surface water mass characteristics described by Lynn and Simpson (1987) include a low-salinity minimum at ~50–100 m depth (Reid *et al*., 1958) close to the coast which indicates the core of the CC.

In the model, the flow results show, consistent with Lynn and Simpson (1987), the presence of southward flow off the Baja Peninsula with significant seasonal variability. For example, in spring and summer (e.g., Figs. 8(b) and (c)), the southward surface jet off the Baja Peninsula is strong along the coast, while during fall and winter (e.g., Figs. 8(a) and (d)) the jet weakens, meanders farther offshore, and is embedded in a more chaotic flow regime. The model also supports maximum southward current speeds of ~20–30 cm/s offshore during spring (e.g., Fig. 8(b)), coincident with the strongest southward wind speeds (Fig. 3(b)). Consistent with the findings of Lynn and Simpson (1987) and Reid *et al*. (1958), the water mass characteristics of the model simulation show that, south of Point Eugenia, a low salinity minimum of ~33.7 (not shown) is present to ~50 m depth.

The region in the vicinity of Point Eugenia, which represents the largest coastline perturbation along the Baja Peninsula, is the location of a seasonally intensifying cyclonic eddy (Lynn and Simpson, 1987). The model upholds Point Eugenia and the region to the south as an area of seasonally intensifying cyclonic meanders and eddies.

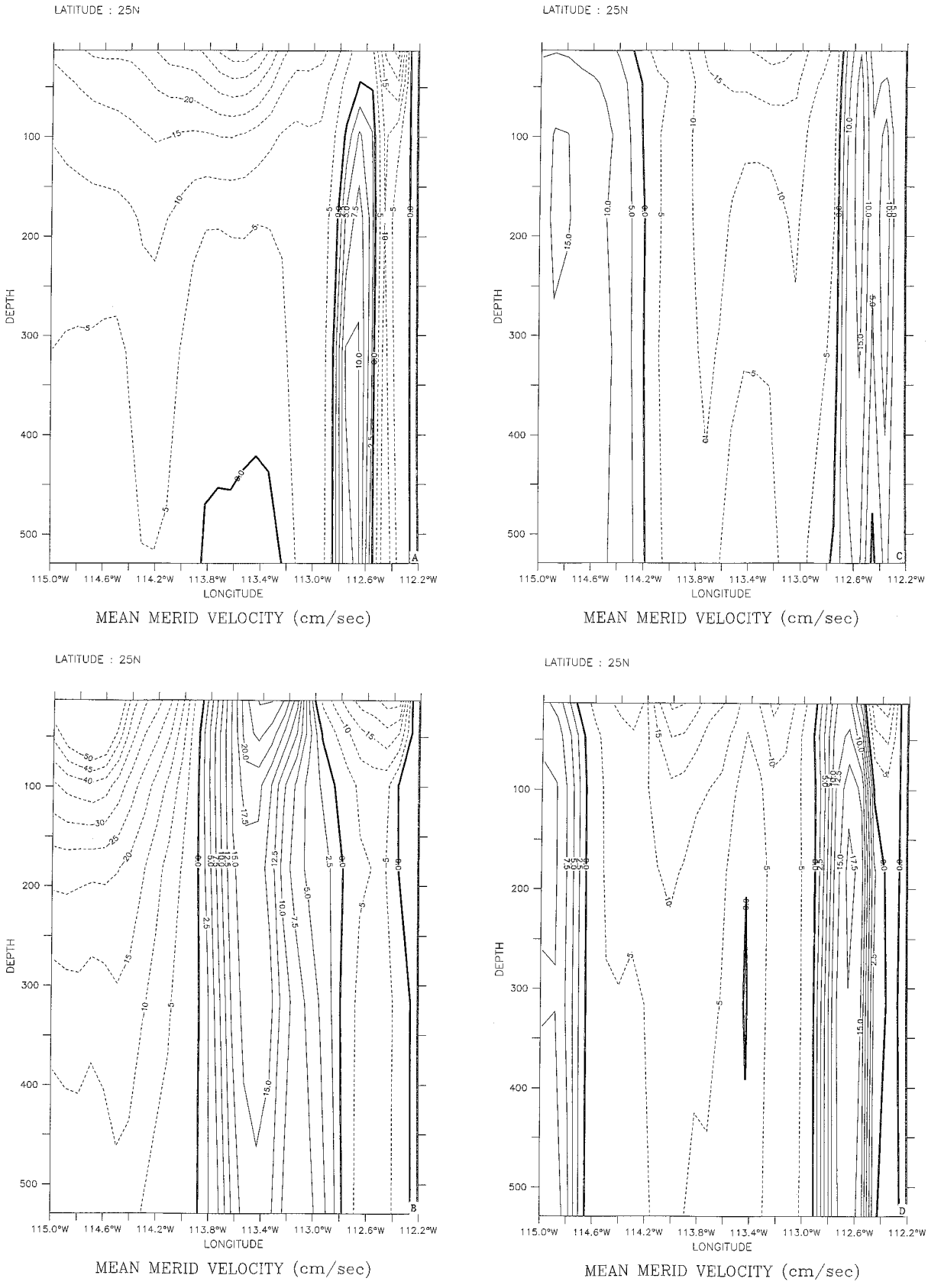

Fig. 11. Cross-shore sections of mean *v* at 25°N (off Cape San Lazaro) for (a) January, (b) April, (c) July, and (d) October of model year 3. The contour interval is 2.5 cm/s (5 cm/s) for northward (southward) flow in (a), (b), (d) and 5 cm/s for both in (c).

For example, in January of year 3 (Fig. 8(a)), a cyclonic meander off Point Eugenia is discernible inshore of where a branch of the southward surface jet has turned away from the coast to rejoin the main stream offshore. In April (Fig. 8(b)), the cyclonic meander has intensified and has begun to detach from the vicinity of Point Eugenia. The meander subsequently closes off to form a cold-core eddy and propagates southwestward (not shown), so that by July (Fig. 8(c)), it is found centered at ~25°N, 118°W. By October (Fig. 8(d)), cyclonic turning to the west-northwest by the southward surface jet has further intensified and approaches the pattern shown for January (Fig. 8(a)). Note that in January (Fig. 8(a)), a cyclonic eddy centered at ~26°N, 123°W is discernible. This eddy also formed as a meander off Point Eugenia the previous year and subsequently propagated southwestward (not shown). Thus, according to model results, Point Eugenia appears to play a significant role in cyclonic eddy generation and subsequent southwestward propagation.

Although a data sparse region, the area off southern Baja is believed to be a highly dynamic environment for meanders, filaments, and eddies (Lynn and Simpson, 1987; Poulain and Niiler, 1989; Niiler *et al*., 1989; Poulain, 1990). Model results support this description for the region south of Point Eugenia. Shoreward anticyclonic meanders in the southward surface jet (Figs. 8(a) and (b)), sharp temperature fronts alongshore and offshore-flowing cold filaments (Figs. 8(c) and (d)), combined with the flow field effects of cyclonic eddies detaching from Point Eugenia to propagate southwestward, all contribute to a highly variable and complicated current structure in the model.

An example of near-surface and subsurface variability in the model for this area is illustrated through cross-sections of mean meridional velocity taken at 25°N, in the vicinity of Cape San Lazaro. In January (Fig. 11(a)), southward flow persists near the surface with core velocities of ~25 cm/s nearshore and ~35 cm/s farther offshore. A northward undercurrent structure is present within ~60 km of the coast with a maximum of ~10 cm/s below ~300 m depth. In April (Fig. 11(b)), southward flow is still present nearshore but adjacent northward flow offshore is now surface-intensified to ~25 cm/s and extends throughout the upper water column, indicating the presence of an anticyclonic eddy nearshore. Farther offshore, the southward jet has intensified to ~50 cm/s in response to the occurrence of maximum southward winds in spring. By July (Fig. 11(c)), alternating northward and southward flow patterns are discernible, which are consistent with the presence of a cyclonic eddy near the coast and an anticyclonic eddy offshore. By October (Fig. 11(d)), the nearshore cyclonic eddy has migrated slightly westward, giving way to a narrow band of surface-intensified southward flow of ~15 cm/s alongshore.

5. Summary and Discussion

This study was designed to investigate the combined role of seasonal wind forcing, seasonal thermohaline gradients, and coastline irregularities on the formation of currents, meanders, eddies, and filaments in the entire California Current System region, from Baja to the Washington-Canada border. Additional objectives were to further characterize the meandering jet south of Cape Blanco and the seasonal variability off Baja. Toward these ends, a high resolution, multi-level primitive equation model using a realistic North American coastline, was forced from rest with spatially and temporally varying winds, temperatures, and salinities. The migration pattern of the North Pacific High, and its effects on the seasonal variability on alongshore winds, was shown to play a significant role in the generation, maintenance, and duration of observed current features throughout the model domain.

Due to the combination of thermohaline gradients and wind forces, different oceanic responses occurred, depending on the season and region. In the winter, in the northward end of the model domain, the combination of onshore geostrophic flow and the onshore Ekman flow resulted in a northward surface coastal current overlying an inshore southward undercurrent, while to the south, weaker onshore geostrophic flow and southward winds resulted in a southward surface coastal current overlying an inshore northward undercurrent. During the upwelling season, the combination of a weakened alongshore pressure gradient and increased southward winds over the entire domain led to a southward surface coastal current overlying an inshore northward undercurrent all along the coast. As the coastal jet and undercurrent became fully established, the currents became unstable and formed meanders, as well as filaments and eddies. In the fall, the return of the northward wind stress and the strengthening of the regional pressure gradients in the northern portion of the model domain resulted in a surfacing of the northward undercurrent and a displacement of the coastal southward jet offshore. To the south, in the fall as in the other seasons, the surface coastal southward jet continued to overlie the northward undercurrent.

The dynamical reasons for the generation and stability of the eddies were also examined using energy transfer analyses. From such analyses, the location and magnitude of barotropic and baroclinic transfers could be found and examined to argue for the type of instability mechanisms which led to the initial eddy generation. The eddies were shown to be generated from instabilities of the California Current and California Undercurrent via barotropic and baroclinic instability processes. For example, in the early eddy generation period, the baroclinic instability process dominated throughout the coastal region except for the region near Point Eugenia, which had barotropic processes comparable to those of baroclinic

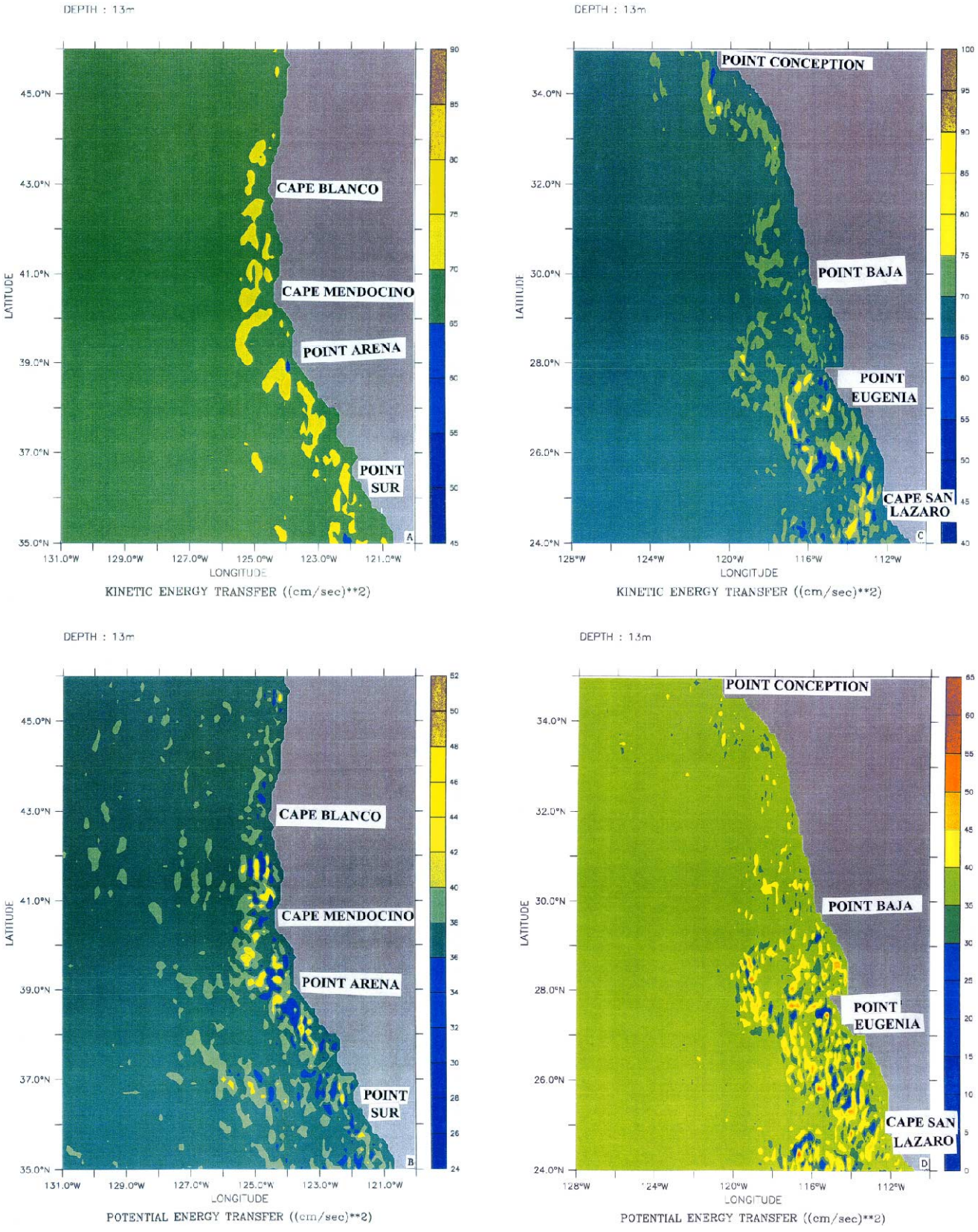

Fig. 12. Horizontal maps at 13 m depth of mean kinetic energy transfers (a), (c) and potential energy transfers (b), (d), averaged over days 270–285, in the northern portion of the domain (a), (b) and the southern portion of the domain (c), (d). Contour interval is 5.0 cm^2/s^2 for (a), (c), and (d), and 2.0 cm^2/s^2 for (b).

instability (not shown). In the later eddy generation period (near the end of the upwelling season), the barotropic instability process was the dominant instability mechanism (i.e., compare Figs. 12(a) and (b)).

Longer run times illustrated the seasonal variability and complex structure of the California Current System. By year 3, the southward surface flow was embedded with numerous eddies, meanders, and upwelling filaments consistent with real-world observations. These eddies and meanders, which propagated westward at Rossby wave speeds, induced relatively large onshore and offshore transports in the southward surface jet. Springtime conditions in the model marked an increase in magnitude of the jet, consistent with Lynn and Simpson (1987). During summer, when upwelling-favorable winds paralleled the coastline throughout the model domain, offshore flowing cold filaments of realistic spatial scales (e.g., Brink and Cowles, 1991) existed in the vicinity of many coastline perturbations. By fall the upwelling system weakened and within the California Bight, a division of flow in the southward jet, first observed in summer, was more pronounced, consistent with a seasonal maxima in the Southern California Eddy (Hickey, 1998).

The coldest water in the model was consistently located adjacent to the southern Baja coastline, coincident with persistent northwesterly winds in the area. The model results support conclusions by Bakun and Nelson (1991) regarding the effects of cyclonic wind stress curl in that the most intense upwelling was located adjacent to capes during spring and summer, and within coastal bights during fall and winter.

Nearshore northward flow occurred throughout the model domain at various depths and intensities during different seasons. These results supported both observational and physical descriptions of seasonal variations in depth, intensity, and extent of northward flow within the California Current System (e.g., Lynn and Simpson, 1987; Hickey, 1998). Specifically, during winter, northward flow primarily maintained an undercurrent structure with a deep core, whereas in summer this flow strengthened and shoaled in many locations.

Maps of mean kinetic energy and eddy kinetic energy were used to indicate mean and eddy energy source locations (Holland *et al*., 1983). The relatively large magnitudes of mean kinetic energy compared to those for eddy kinetic energy were consistent with the hypothesis that eddies are driven by the mean flow instead of the mean flow driving the eddies. Model results showed maxima in mean and eddy kinetic energy during the upwelling season wherever flow velocity increased, such as along the meandering axis of the southward coastal jet as well as in the vicinity of westward propagating eddies. The eddy kinetic energy maxima tended to propagate westward with time, consistent with Kelly *et al*. (1998), and disclosed eddy generation areas off Cape Blanco, offshore and downstream of Cape Mendocino and Point Arena, in the Southern California Bight, and in the coastal indentations on either side of Point Eugenia.

With the larger model domain, the model results supported the meandering southward jet as a continuous feature from south of Cape Blanco to Baja. The jet also marked a division between cold, upwelled, coastally-influenced water and water of offshore origin. The jet remained within close proximity of the coast north of Cape Blanco. South of Cape Blanco, the jet underwent a series of cyclonic and anticyclonic excursions as coastline perturbations became more pronounced. As it proceeded southward, meander activity increased and the region of coastally influenced water widened. Mixing of coastal and offshore waters took place through offshore-flowing cold filaments and westward propagating eddies.

The model reproduced many surface, near-surface, and subsurface characteristics off the Baja Peninsula described by Lynn and Simpson (1987). In spring and summer, the southward surface jet off Baja was strong and located closer to the coast. Conversely, during fall and winter, the jet weakened, meandered farther offshore, and was embedded in a more chaotic flow regime. Vertical salinity distributions (not shown) illustrated the fresher, near-surface flow of the southward jet offshore, as well as the influx of more saline Southern Water with the northward undercurrent near the coast. The belief that strong seasonal variations in positions and intensities of atmospheric forcing mechanisms produced a complex and highly variable flow regime off southern Baja was well supported by the model. The area off southern Baja was shown to be a highly dynamic environment for meanders, filaments, and eddies, while the area off Point Eugenia, which represents the largest coastline perturbation along the Baja peninsula, was shown to be a persistent cyclonic eddy generation region.

Overall, the results from this model simulation showed that the inclusion of a realistic coastline from Baja to the Washington-Canada border, spatially and temporally varying wind forcing, and thermohaline gradients are key mechanisms for the generation, evolution, and maintenance of all of the major currents of the California Current System (i.e., the California Current, the California Undercurrent, the Davidson Current, the Southern California Countercurrent, and the Southern California Eddy), as well as for the generation of intense and complex meander, eddy and filament structures in the California Current System.

Appendix: Energy Analysis

An energy analysis based on that of Han (1975), Semtner and Mintz (1977) and Batteen *et al*. (1992) is made to gain a better understanding of the energy trans-

fers in the unstable flow. The energy transfers are presented using the Semtner and Mintz (1977) notation:

- $(\bar{})$ time average
- $(\,)'$ time deviation
- $(\tilde{})$ horizontal space average
- $(\,)^*$ horizontal space deviation.

The kinetic energy (K') is calculated by

$$K = \frac{u^2 + v^2}{2} \tag{A1}$$

and presented in a time series plot. After reaching a quasi-steady state in which the total kinetic energy is nearly constant, the time mean and time eddy kinetic energy are calculated by

$$\overline{K} = \frac{\overline{u^2} + \overline{v^2}}{2} \tag{A2}$$

$$K' = \frac{\overline{u'^2} + \overline{v'^2}}{2}. \tag{A3}$$

Available potential energy (P) is calculated by

$$P = \alpha g \left[\frac{1}{2} \left(T^* \right)^2 \left(\frac{\partial \tilde{T}}{\partial z} \right)^{-1} \right] \tag{A4}$$

and plotted in a time series to determine when a quasi-steady state is reached and statistics can be collected. The temporal mean and eddy available potential energy are then calculated by

$$\overline{P} = \alpha g \left[\frac{1}{2} \overline{\left(T^* \right)^2} \left(\frac{\partial \bar{\tilde{T}}}{\partial z} \right)^{-1} \right] \tag{A5}$$

$$P' = \alpha g \left[\frac{1}{2} \overline{\left(T'^* \right)^2} \left(\frac{\partial \bar{\tilde{T}}}{\partial z} \right)^{-1} \right]. \tag{A6}$$

The transfers between the energy types are defined, after Semtner and Mintz (1977), by

$$\left\{ \overline{K} \rightarrow \overline{P} \right\} = -\alpha g \left[\overline{T} \overline{w} \right] \tag{A7}$$

$$\left\{ P' \rightarrow K' \right\} = \alpha g \left[\overline{T' w'} \right] \tag{A8}$$

$$\left\{ \overline{K} \rightarrow K' \right\} = \bar{v} \cdot \left(\nabla \cdot \overline{v'v'} + \frac{\partial}{\partial z} \overline{w'v'} \right) \tag{A9}$$

$$\left\{ \overline{P} \rightarrow P' \right\} = \alpha g \left[\overline{T^*} \nabla \cdot \overline{v' T'^*} \left(\frac{\partial \bar{\tilde{T}}}{\partial z} \right)^{-1} \right]. \tag{A10}$$

Using the energy transfers calculated above and the temporal mean and eddy kinetic and available potential energy values, energy transfers are calculated for those periods in which the total energies are nearly constant and used to argue for the instability mechanism that leads to the initial eddy generation (e.g., see Figs. 12(a) and (b)).

References

Bakun, A. and C. S. Nelson (1991): The seasonal cycle of wind stress curl in subtropical eastern boundary current regions. *J. Phys. Oceanogr.*, **21**, 1815–1834.

Barth, J. A. and R. L. Smith (1996a): Separation of a coastal upwelling jet and pathways for cross-shelf exchange: a Lagrangian perspective. *EOS, Trans. Am. Geophys. Union*, Ocean Sciences Meeting Supplement, OS 130.

Barth, J. A. and R. L. Smith (1996b): Coastal ocean circulation off Oregon: recent observations of spatial and temporal variability. In *Estuarine and Ocean Survival of Northeastern Pacific Salmon: A Workshop and Extended Abstracts*, NOAA Technical Memorandum, NMFS, NWFSC.

Barth, J. A., R. L. Smith and A. Huyer (1994): Separation of a coastal jet and cyclogenesis during coastal upwelling. *EOS, Trans. Am. Geophys. Union*, 1994 Fall Meeting Supplement, 345.

Batteen, M. L. (1997): Wind-forced modeling studies of currents, meanders, and eddies in the California Current System. *J. Geophys. Res.*, **102**, 985–1009.

Batteen, M. L. and P. W. Vance (1998): Modeling studies of the effects of wind forcing and thermohaline gradients in the California Current System. *Deep-Sea Res. II*, **45**, 1507–1556.

Batteen, M. L., M. J. Rutherford and E. J Bayler (1992): A numerical study of wind and thermal forcing effects on the ocean circulation off Western Australia. *J. Phys. Oceanogr.*, **22**, 1406–1433.

Batteen, M. L., C. A. Collins, C. R. Gunderson and C. S. Nelson (1995): The effect of salinity on density in the California Current System. *J. Geophys. Res.*, **100**, 8733–8749.

Bernstein, R. L., L. C. Breaker and R. Whritner (1977): California Current eddy formation: Ship, air, and satellite results. *Science*, **195**, 353–359.

Brink, K. H. and T. J. Cowles (1991): The Coastal Transition Zone program. *J. Geophys. Res.*, **96**, 14,637–14,647.

Chelton, D. B. (1984): Seasonal variability of alongshore geostrophic velocity off central California. *J. Geophys. Res.*, **89**, 3473–3486.

Davis, R. E. (1985): Drifter observations of coastal surface

currents during CODE: The method and descriptive view. *J. Geophys. Res*., **90**, 4741–4755.

Haidvogel, D. B., A. Beckman and K. S. Hedstrom (1991): Dynamical simulation of filament formation and evolution in the coastal transition zone. *J. Geophys. Res*., **96**, 15017–15040.

Han, Y.-J. (1975): Numerical simulation of mesoscale eddies. Ph.D. Thesis, University of California, Los Angeles, 154 pp.

Hickey, B. M. (1979): The California Current System-Hypotheses and facts. *Prog. Oceanogr*., **8**, 191–279.

Hickey, B. M. (1998): Coastal oceanography of western North America, from the tip of Baja California to Vancouver Island. p. 345–393. In *The Sea*, Vol. 11, John Wiley & Sons Inc., New York, 1062 pp.

Holland, W. R., D. E. Harrison and A. J. Semtner, Jr. (1983): Eddy-resolving numerical models of large-scale ocean circulation. p. 379–404. In *Eddies in Marine Science*, Springer-Verlag, New York, 609 pp.

Ikeda, M., L. A. Mysak and W. J. Emery (1984): Observations and modeling of satellite-sensed meanders and eddies off Vancouver Island. *J. Phys. Oceanogr*., **14**, 3–21.

Kelly, K. A., R. C. Beardsley, R. Lineburner, K. H. Brink, J. D. Paduan and T. K. Chereskin (1998): Variability of near-surface eddy kinetic energy in the California Current based on altimetric, drifter, and moored current data. *J. Geophys. Res*., **103**, 13,067–13,083.

Levitus, S. and T. P. Boyer (1994): World Ocean Atlas 1994, Volume 4: Temperature. *NOAA Atlas NESDI 4*, U.S. Department of Commerce, Washington, D.C., 117 pp.

Levitus, S., R. Burgett and T. P. Boyer (1994): World Ocean Atlas 1994, Volume 3: Salinity. *NOAA Atlas NESDI 3*, U.S. Department of Commerce, Washington D.C., 99 pp.

Lynn, R. S. and J. J. Simpson (1987): The California Current System: The seasonal variability of its physical characteristics. *J. Geophys. Res*., **92**, 12947–12966.

Niiler, P. P., P.-M. Poulain and L. R. Haury (1989): Synoptic three-dimensional circulation in an onshore-flowing filament of the California Current. *Deep-Sea Res*., **36**(3), 385–405.

Poulain, P.-M. (1990): Near-inertial and diurnal motions in the trajectories of mixed layer drifters. *J. Mar. Res*., **48**, 793–823.

Poulain, P.-M. and P. P. Niiler (1989): Statistical analysis of the surface circulation in the California Current System using satellite-tracked drifters. *J. Phys. Oceanogr*., **19**(10), 1588–1603.

Reid, J. L., Jr. (1963): Measurements of the California Countercurrent off Baja California. *J. Geophys. Res*., **68**, 4819–4822.

Reid, J. L. Jr., G. I. Roden and J. G. Wyllie (1958): Studies of the California Current System. CalCOFI Rep. 6, California Cooperative Oceanic Fisheries Investigation, La Jolla, pp. 27–56.

Semtner, A. J. and Y. Mintz (1977): Numerical simulation of the Gulf Stream and midocean eddies. *J. Geophys. Res*., **7**, 208–230.

Strub, P. T. and C. James (1995): The large-scale summer circulation of the California Current. *Geophys. Res. Lett*., **22**, 207–210.

Strub, P. T., C. James, A. C. Thomas and M. R. Abbott (1990): Seasonal and nonseasonal variability of satellite-derived surface pigment concentration in the California Current. *J. Geophys. Res*., **95**(C1), 11501–11530.

Strub, P. T., P. M. Kosro, A. Huyer and CTZ Collaborators (1991): The nature of the cold filaments in the California Current System. *J. Geophys. Res*., **96**, 14743–14768.

Strub, P. T., T. K. Chereskin, P. P. Niiler, C. James and M. D. Leveine (1997): Altimeter-derived variability of surface velocities in the California Current System, 1, Evaluation of TOPEX altimeter velocity resolution. *J. Geophys. Res*., **102**, 727–748.

Trenberth, K. E., W. G. Large and J. G. Olsen (1990): The mean annual cycle in global ocean wind stress. *J. Phys. Oceanogr*., **20**, 1742–1760.